Rapid solidification of silver-rich Ag–Cu–Zr–Al alloys

A. Castellero [a,*], G. Angella [b], M. Vedani [c], M. Baricco [a]

[a] Dipartimento di Chimica and NIS, Università di Torino, Torino, Italy
[b] Istituto per l'Energetica e le Interfasi, CNR-IENI, Milano, Italy
[c] Dipartimento di Meccanica, Politecnico di Milano, Milano, Italy

Available online 29 November 2012

1. Introduction

Phase separation in a liquid alloy occurs when at least a pair of components (e.g. Cu–Pb) have a positive enthalpy of mixing. Such a miscibility gap can be either thermodynamically metastable or stable, such as in the case of Co–Cu [1] and Cu–Pb [2], respectively. In the first case, phase separation occurs only by promoting the undercooling of the liquid. Different length scales in the microstructure can be produced in undercooled immiscible liquid alloys depending on the transformation mechanism which occurs: Interconnected fractal microstructures are the result of a continuous transformation such as the spinodal decomposition, whereas droplet-type microstructures derive from a nucleation and growth process [3].

Alloys showing liquid phase separation have interesting properties in view of potential applications, even if industrial production using this process is rather limited because of the difficulty in obtaining uniform and finely dispersed microstructures. For example, dispersion hardening can be achieved by a fine and uniform dispersion of hard particles in a ductile matrix as a result of the hindered movement of the dislocations [4]. On the contrary, dispersion of a soft phase in a high strength matrix allows to design advanced bearing materials [4]. A common industrial application is the dispersion of Pb particles at the grain boundaries in brass, as a consequence of the miscibility gaps in the Cu–Pb and Zn–Pb binary systems, in order to favor the machining of the material through a fine fragmentation of the chips.

A step forward towards the development of smart materials has been represented by the exploitation of liquid phase separation in glass forming alloys [5]. In these systems, amorphous/amorphous composite microstructures can be formed when both liquids have a good glass forming ability [5]. If only one liquid is a good glass former, amorphous/crystalline composites can be obtained [6]. For example, Park et al. [7]. studied a phase-separated Nd–Zr–Al–Co metallic glass with combined hard and soft magnetic properties, Gebert et al. [8] have investigated chemical and electrochemical reactivity of a phase-separated Ni–Nb–Y metallic glass, Jayaraj et al. [9] obtained a nano-porous Ti-based amorphous alloy by selective dissolution of the Y-rich amorphous phase in the $Y_{20}Ti_{36}Al_{24}Co_{20}$ two-phase metallic glass.

In these systems, the presence of a second phase (either amorphous or crystalline), favors the shear delocalization by branching the individual shear bands and tends to stop their propagation, provided that a strong and intimate interface between the two phases is formed. The strain at failure of amorphous/crystalline composites depends on the volume fraction, size, shape and distribution of the second phase inclusions [10–14]. In the case of composites containing micron sized ductile crystalline particles finely dispersed in the amorphous matrix, the propagation of shear bands is confined by the interparticle distance [10] and the deformation of the ductile crystalline particles occurs by conventional dislocation mechanism [11], enabling plastic deformation either

* Corresponding author. Tel.: +39 011 670 7097; fax: +39 011 670 7855.
E-mail address: alberto.castellero@unito.it (A. Castellero).

in compression and tension [12]. Plastic deformation of the composites can be further improved when the second phase precipitates have a spherical shape instead of a dendritic morphology [13] because of the reduced stress concentration at the interface between the two phases. Initiation of multiple shear bands can be also promoted by a fine dispersion of nanocrystalline particles. However, in this case, the propagation of shear bands is not inhibited because the particles size is of the same order of magnitude with respect to the shear band width [15,16].

In this paper we investigated the effect of Al addition to the Ag–Cu–Zr ternary system with the aim of obtaining silver-rich (80 wt.%) amorphous/crystalline composites, exploiting the liquid miscibility gap in Ag–Cu–Zr [17,18]. In a previous study [19], we reported that rapid solidification of Ag-rich Ag–Cu–Zr alloys promotes, on the one hand, the crystallization of a ductile f.c.c.-Ag solid solution from the Ag-rich liquid, and, on the other hand, amorphization of the Ag-poor liquid, as a consequence of the good glass forming ability in the Cu–Zr–Ag system for Ag contents lower than 40 at.% [20,21]. The phase selection and the microstructures of four different alloys obtained at different cooling rates were interpreted on the basis of the equilibrium Ag–Cu–Zr [17] and Cu–Zr–Al ternary phase diagrams [22].

2. Experimental

Alloys with nominal composition (at.%) $Ag_{73.0}Cu_{12.7}Zr_{12.1}Al_{2.2}$ (alloy A), $Ag_{73.1}Cu_{17.2}Zr_{9.7}$ (alloy B0), $Ag_{72.5}Cu_{16.7}Zr_{9.4}Al_{1.4}$ (alloy B1), $Ag_{71.8}Cu_{16.2}Zr_{9.1}Al_{2.8}$ (alloy B2) were designed in such a way to fulfill the silver content (80 wt.%) in commercial precious alloys. Alloy A was designed by combining pure silver with $Cu_{47}Zr_{45}Al_8$ (at.%), which is known to be one of the best glass formers compositions in the Cu–Zr–Al ternary system [23]. Alloys B0, B1 and B2, are characterized by a constant Cu:Zr ratio 64:36, that corresponds to the best glass former in the binary Cu–Zr system [24]. In alloys B1 and B2, Cu and Zr were partially substituted by Al in order to evaluate its effect on the glass forming ability of the Ag-poor liquid.

Master alloys were prepared by arc melting the pure elements under Ar atmosphere. Each ingot was re-melted several times in order to obtain a good homogeneity. Rapid solidified ribbons (about 40 μm thick) were obtained by planar flow casting using a wheel speed of 15 m/s in Ar atmosphere. In the case of alloy A. thinner ribbons (about 20–25 μm thick) were obtained by melt spinning using a wheel speed of 30 m/s in Ar atmosphere.

A PANalytical X'Pert X-ray diffractometer (XRD) with Cu K_α radiation was used for structural characterization. For rapidly solidified ribbons, the analysis has been carried out on the side in contact with the quenching wheel. The microstructure of master alloys and as-spun ribbons was observed with a Leica Stereoscan 410 scanning electron microscope (SEM) equipped with an energy dispersion spectroscopy (EDS) microprobe (Oxford Instruments). An image analysis of the backscattered SEM images was performed in order to evaluated the volume fraction of the bright Ag-rich phase and the dark Ag-poor phase mixture. The average composition of the dark Ag-poor phase mixture was estimated from the material balance for each component expressed in the following way:

$$x_T^i = x_B^i y_B + x_D^i (1 - y_B) \quad (1)$$

with

$$y_B = \frac{V_B \rho_B}{V_B \rho_B + (1 - V_B)\rho_D} \quad (2)$$

$$\rho_D = \frac{1}{\sum_{i=1}^{n} \frac{x_D^i}{\rho_i}} \quad (3)$$

$$\rho_B = \frac{1}{\sum_{i=1}^{n} \frac{x_B^i}{\rho_i}} \quad (4)$$

where x_T^i, x_B^i and x_D^i are the mass fractions of the ith component measured by EDS in the total scanned area (T), in the bright Ag-rich area (B) and in the dark Ag-poor area (D), respectively; V_B is the volume fraction of the bright Ag-rich phase in the scanned area; ρ_B and ρ_D are the densities of the bright and dark areas, respectively, calculated as the weighted average of the density of each element, ρ_i. The unknown quantities x_D^i were determined by solving a system of n equations.

The thermal stability of the as-spun ribbons was characterized by differential scanning calorimetry at 20 °C/min using a Perkin Elmer DSC 7. Hardness of the as quenched ribbons was evaluated by instrumented indentation using a load controlled Fischerscope HM2000 with a Vickers diamond pyramid. Indents with depth of 0.5 μm were performed with a loading rate of 0.5 mN/s. At least nine measurements were performed for each indentation series. For all the samples hardness and indentation modulus values were extracted according to the standard ISO 14557-1. The capability of the ribbon to be plastically deformed was qualitatively estimated by bending test. Fracture surfaces, produced by a tensile test under controlled deformation rate, were observed by SEM. For comparison, also the Vickers hardness of a commercial Ag–20 wt.% Cu alloy was measured, using a Buehler microhardness tester with a load of 100 gf.

3. Results

Microstructures of the master alloys, obtained by backscattered electron detector, are shown by the SEM micrographs in Fig. 1. Corresponding X-ray diffraction patterns are shown in Fig. 2(a). At low magnification, all samples show clear evidence of phase separation in the liquid with dark Ag-poor droplets dispersed in a bright Ag-rich matrix, and bright Ag-rich droplets embedded in larger dark Ag-poor droplets. In master alloy B0 and B1, Fig. 1(a) and Fig. 1(b) respectively, the presence of Ag-rich dendrites in the dark droplets indicates that solidification occurred in an undercooled liquid. The combination of the information from the EDS analysis on the single phases performed at higher magnification (see insets of Fig. 1) and the results of the XRD patterns, Fig. 2(a), allowed to identify the following crystalline phases in the master alloys: f.c.c.-Ag, CuZr, $CuZr_2$, AgZr and τ_5-$Al_{2-x}Cu_xZr$ in alloy A; f.c.c.-Ag, $Cu_{10}Zr_7$, $AgCu_4Zr$ (m-phase), AgZr and $CuZr_2$ in alloy B0; f.c.c.-Ag, $Cu_{10}Zr_7$, $CuZr_2$ and τ_4-$AlCu_2Zr$ in alloy B1 and alloy B2.

The combination of the image and the EDS analyses allowed to determine the following average compositions (with a maximum standard deviation of 4 at.%) for the dark droplets in the master alloys: $Ag_{24}Cu_{33}Zr_{37}Al_6$ for alloy A, $Ag_{18}Cu_{48}Zr_{34}$ for alloy B0, $Ag_{17}Cu_{46}Zr_{33}Al_4$ for alloy B1, $Ag_{17}Cu_{42}Zr_{33}Al_8$ for alloy B2. The bright Ag-rich phase (f.c.c. solid solution) contains in average about 4 ± 1 at.% of Cu, whereas the amount of the other elements is below the detection limit of the EDS technique (<1 at.%). As a consequence of the dissolution of Cu in the f.c.c.-Ag solid solution, the Cu:Zr ratio in the dark droplets becomes slightly lower with respect to the nominal one.

The effect of rapid solidification by planar flow casting on phase selection and microstructure is shown by the XRD patterns of Fig. 2(b) and the SEM micrographs of Fig. 3, respectively. For B0, B1 and B2 alloys, the crystallographic reflections of the intermetallic phases show a lower relative intensity after quenching with respect to those of the corresponding master alloy. In alloy A, when the wheel speed is increased to 30 m/s only the crystallographic reflections belonging to the f.c.c.-Ag solid solutions are present (dotted vertical lines) and the formation of the intermetallic phases, observed after quenching at 15 m/s, is suppressed.

After rapid solidification, the microstructures of the as-spun ribbons, shown by the backscattered electrons images in Fig. 3, are significantly finer with respect to those corresponding to master alloys (Fig. 1). All ribbons show a microstructural gradient with a progressive size increase of the Ag-poor dark droplets from the wheel side towards the free side of the ribbon. In the case of alloy A, the faster quenching at 30 m/s produces a significantly finer microstructure, Fig. 3(e), because of the higher quenching rate. The elongated shape of the dark droplets in the bright matrix is caused by the shear flow of the two phase-separated liquids [25], induced by the quenching process onto the wheel.

An indexing of the crystallographic reflections of Fig. 2(b), combined with the EDS analysis of the larger dark Ag-poor droplets on the free side of the ribbon, allowed to identify the following crystalline phases in the as quenched ribbons: f.c.c.-Ag in alloy A quenched at 30 m/s; f.c.c.-Ag, CuZr, $CuZr_2$ and τ_5 in alloy A quenched at 15 m/s; f.c.c.-Ag in alloy B0 quenched at 15 m/s; f.c.c.-Ag, CuZr, $CuZr_2$ and $Cu_{10}Zr_7$ in alloy B1 quenched at 15 m/s; f.c.c.-Ag, CuZr, $CuZr_2$, $Cu_{10}Zr_7$ and τ_4 in alloy B2 quenched at 15 m/s.

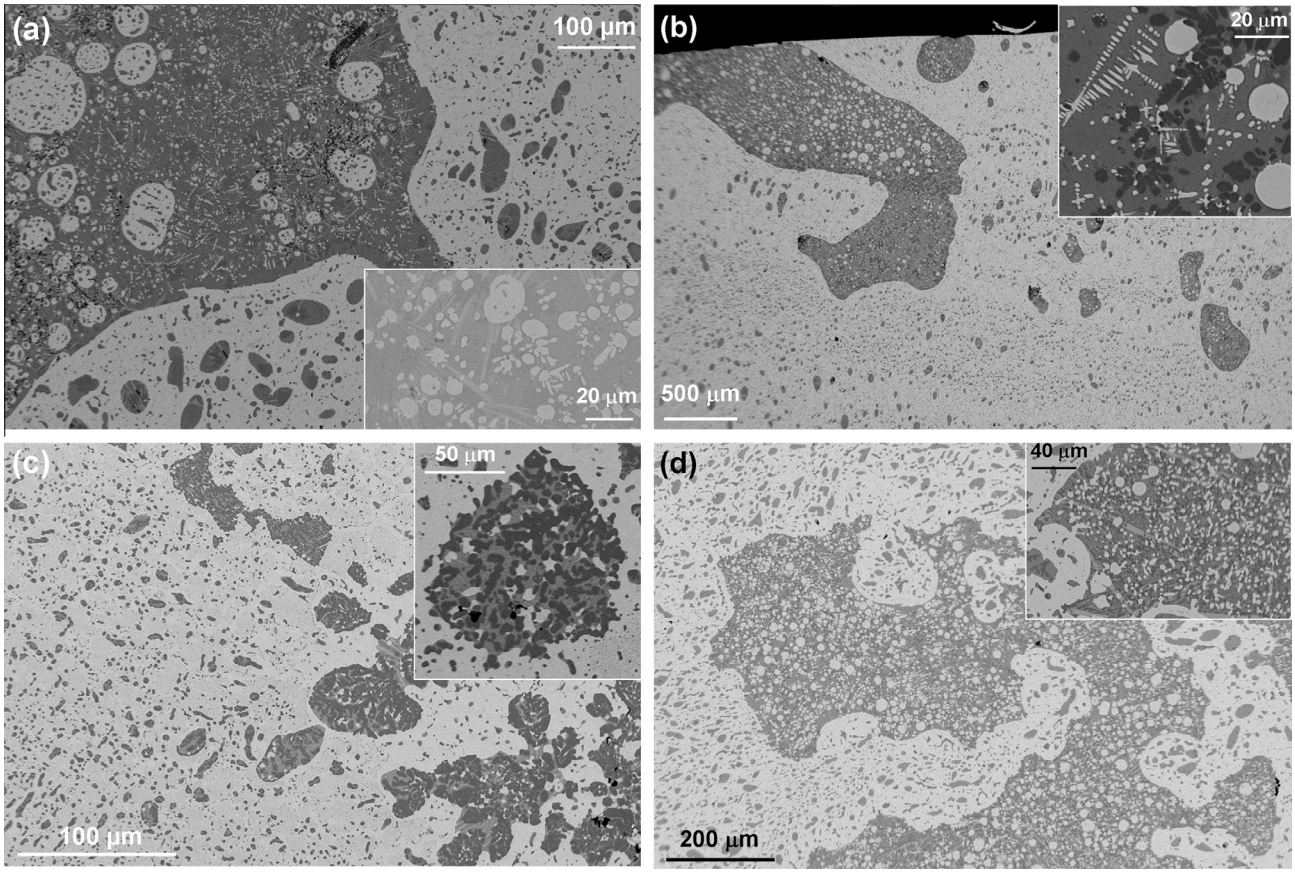

Fig. 1. SEM micrographs (backscattered electrons signal) of the master alloys: alloy B0 (a), alloy B1 (b), alloy B2 (c), and alloy A (d).

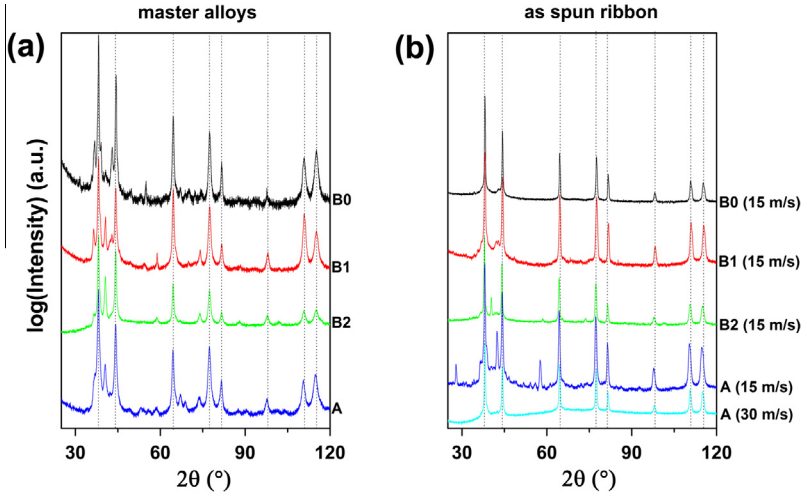

Fig. 2. XRD patterns (Cu K_α) of the master alloys (a) and the as-spun ribbons (b). The vertical dotted lines indicate the position of the crystallographic reflections of the f.c.c.-Ag solid solution.

The DSC traces of the as-spun ribbons are shown in Fig. 4. In the case of alloy B0, the DSC trace shows a clear glass transition at 415 °C, followed by an exothermic peak starting (T_{onset}) at 471 °C with a peak temperature (T_{peak}) at 484 °C and the crystallization enthalpy (ΔH_x) of 9.2 J/g. This peak is related to a small amount of an amorphous phase that could not be detected by X-ray diffraction analysis, because of the overlapping of the amorphous halo with the very intense crystallographic reflections of the f.c.c. Ag solid solution. In alloy B1, the glass transition shifts to 418 °C and the main crystallization peak (T_{onset} = 489 °C, T_{peak} = 497 °C, ΔH_x = 7.0 - J/g) is preceded by a shoulder at lower temperature. For alloy B2, there is no sign of a glass transition, but a crystallization peak can be clearly evidenced (T_{onset} = 467 °C, T_{peak} = 481 °C, ΔH_x = 1.4 - J/g). In alloy A quenched at 15 m/s, a weak exothermic peak (ΔH_x = 0.4 J/g) starts at 456 °C with a peak at 471 °C. Finally, when the wheel speed is increased to 30 m/s, the as-spun ribbon of alloy A shows a glass transition at 453 °C, followed by a crystallization event (T_{onset} = 485 °C, T_{peak} = 497 °C, ΔH_x = 5.2 J/g).

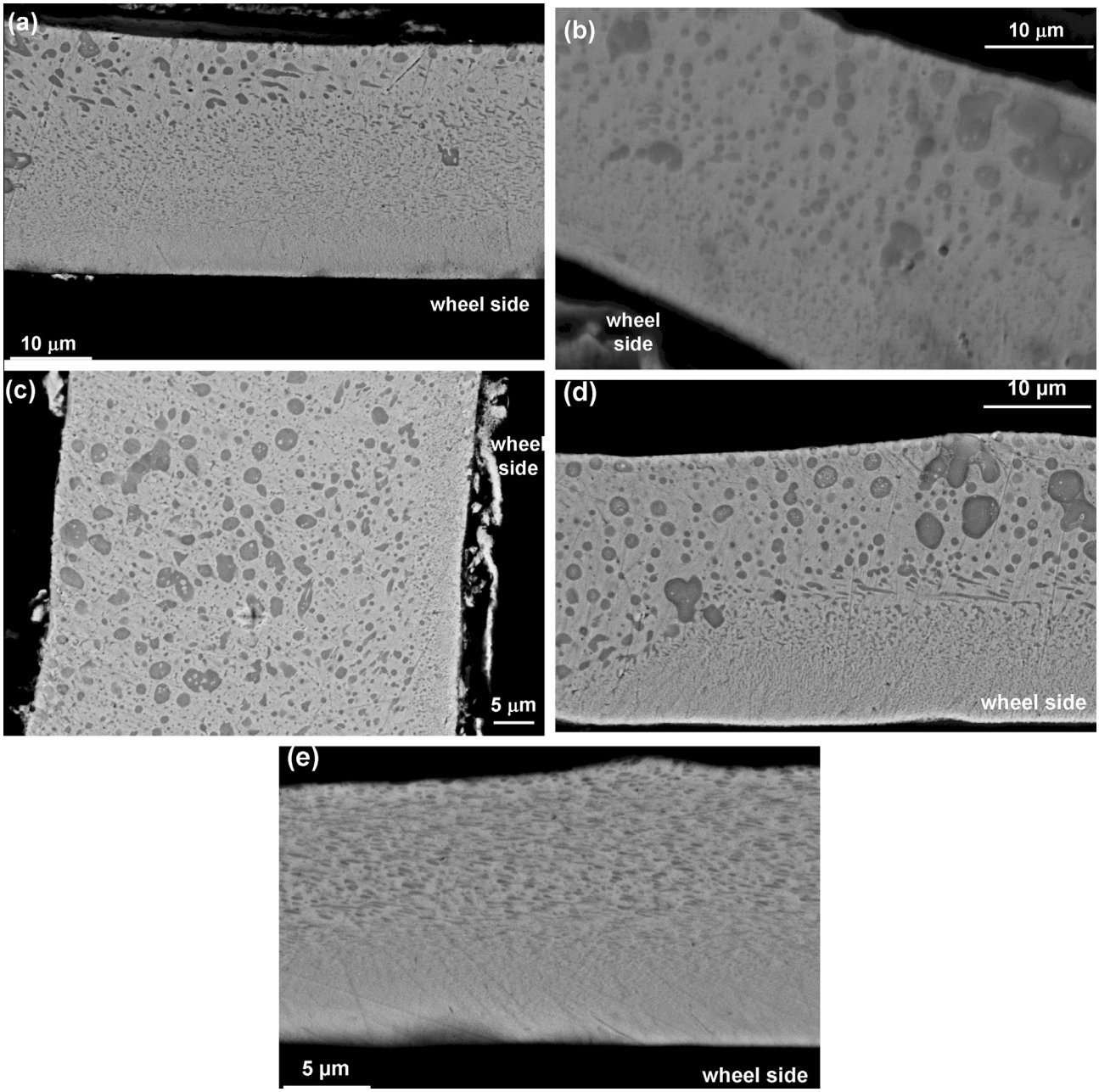

Fig. 3. SEM micrographs (backscattered electrons signal) of the as-spun ribbons: alloy B0 (a), alloy B1 (b), alloy B2 (c), alloy A (d–e). Micrographs (a–d) refer to ribbons quenched at 15 m/s, micrograph (e) refers to a ribbon quenched at 30 m/s.

The values of hardness and indentation Young modulus for the as-spun ribbons are reported in Table 1. As a consequence of the statistical dispersion of the values, it can be assumed all four as quenched alloys have similar hardness and modulus. All the alloys show a ductile behavior upon bending. The fracture surface of as-spun ribbons after tensile test are shown in Fig. 5(a) and (b) for alloys B0 and B1, respectively. In alloy B0, the failure occurs with a typical ductile behavior with the presence of dimples on the fracture surface, related to the elongation of the ductile f.c.c.-Ag solid solution. In alloys B1, the fracture surface shows micron size particles belonging to the $CuZr_2$ intermetallic compound, embedded in the f.c.c.-Ag solid solution, that failed with a typical brittle behavior, as evidenced by the cleavage features in the particle on the right side of Fig. 5(b). In some cases, small amounts of the f.c.c.-Ag solid solution can be observed on the smooth surface of the $CuZr_2$ particles, left side of Fig. 5(b), suggesting a de-bonding of the matrix from the intermetallic compound before failure of the brittle phase.

4. Discussion

The observed phase selection and microstructures obtained under different cooling rates (slowly cooled master alloy and rapidly quenched ribbons) can be explained on the basis of the Ag–Cu–Zr [17,19] and Cu–Zr–Al [22] ternary phase diagrams.

In the dark Ag-poor droplets of master alloy B0, on the basis of the estimated average composition ($Ag_{18}Cu_{48}Zr_{34}$), the expected equilibrium phases are AgZr, $CuZr_2$ and $Cu_{10}Zr_7$, as effectively observed by XRD and SEM. The presence of the m-phase was explained considering the undercooling occurring in different regions of the liquid, leading to different solidification paths depending on the composition of the undercooled liquids [19].

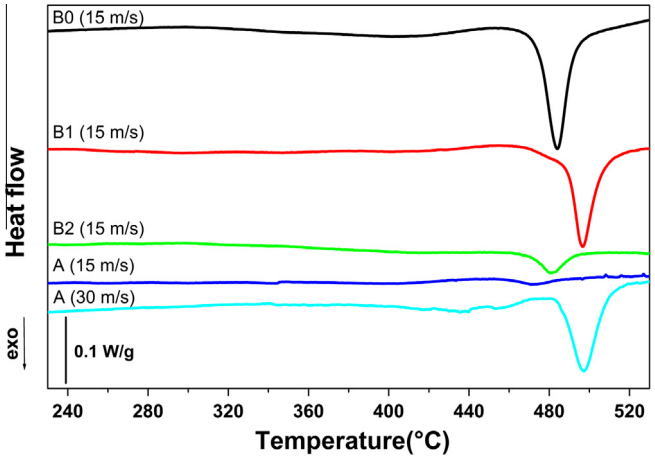

Fig. 4. DSC traces of the as-spun ribbons at a heating rate of 20 °C/min.

Table 1
Vickers hardness and Young indentation modulus values for the as-spun ribbons. Indents with constant depth (0.5 m) were performed at a loading rate of 0.5 mN/s.

	Vickers hardness (HVN)	Indentation modulus (GPa)
Alloy A	292 ± 15	94 ± 6
Alloy B0	260 ± 48	90 ± 6
Alloy B1	265 ± 22	93 ± 3
Alloy B2	277 ± 40	89 ± 4

The partial substitution of Cu and Zr with Al in master alloys B1 and B2 inhibits the formation of the AgZr intermetallic compound, that induces brittleness when it solidifies as a primary phase [19]. If it is assumed that, as a consequence of the liquid phase separation, the Ag content in the Ag-poor liquid is negligible, the observed phases ($Cu_{10}Zr_7$, $CuZr_2$ and τ_4-$AlCu_2Zr$) in the dark droplets are those expected according to the equilibrium Cu–Zr–Al ternary diagram [22].

In master alloy A, the AgZr phase is stabilized by the lower Cu:Zr ratio with respect to alloys B1 and B2. As in the case of alloys B1 and B2, the observed phases (CuZr, $CuZr_2$ and τ_4-$AlCu_2Zr$) in the dark droplets are those expected according to the equilibrium Cu–Zr–Al ternary diagram [22] when the presence of silver is neglected. However, the presence of CuZr instead of $Cu_{10}Zr_7$ indicates the tendency of the Ag-poor liquid to be undercooled, since the former phase is stable only at high temperature whereas the latter phase is stable at room temperature.

The effect of rapid solidification on the phase selection depends either on the Al content and the quenching rate. In absence of Al (alloy B0), quenching at 15 m/s inhibits the formation of the intermetallic phases observed in the master alloys, whereas when Al is added (alloys B1 and B2) the as-spun ribbons contain a significant amount of intermetallic phases, as detected by X-ray diffraction analysis (Fig. 2(b)). In alloy A, the intermetallic phases observed after quenching at 15 m/s do not form when the wheel speed is increased up to 30 m/s. The suppression of the intermetallic phases is confirmed by the formation of a higher amount of amorphous phase, as shown by the DSC analysis (Fig. 4). The estimated compositions in the dark droplets of the master alloys, indicate that the Ag-poor liquid is pushed out from the equilibrium composition range [17,18], suggesting a tendency of the liquid to be undercooled even at the relatively low cooling rates obtained in the arc furnace. In alloy B0, that does not contain Al, the composition of the Ag-poor dark droplets falls well inside the glass forming composition range of the Ag–Cu–Zr ternary system [17,21], accounting for the formation of the amorphous phase detected by DSC.

Concerning the mechanical properties, the bending ductility of the ribbons of all four alloys can be explained by the presence of a continuous network of the ductile matrix of the f.c.c.-Ag solid solution. Furthermore, the rounded interface between the matrix and the intermetallic compounds likely reduces the stress concentration and inhibits the crack propagation. The presence of either hard intermetallic compounds and amorphous phase in the as quenched ribbons of the different alloys brings to hardness values between 260 and 290 HV, that turns out significantly higher than those of commercially pure silver, 99.98%, (45 ± 3 HV for the annealed state) [26] and the commercial Ag-20 wt.% Cu alloy (87 ± 2 HV for the annealed state).

5. Conclusions

In this work, the synthesis of amorphous/crystalline Ag–Cu–Zr–Al composites containing 80 wt.% Ag was achieved by rapid solidification, exploiting the phase separation into Ag-rich and (Cu, Zr, Al)-rich liquids.

Image analysis of microstructures of master alloys, combined with EDS analysis, revealed that the average composition of the Ag-poor regions are off the equilibrium composition range of the miscibility gap, suggesting that a significant undercooling of the liquid already occurred at moderately low cooling rates in the arc furnace.

Rapidly quenched ribbons consist of a mixed amorphous/crystalline microstructure, showing that it is possible to retain the (Cu, Zr, Al)-rich amorphous phase in the Ag-rich crystalline matrix. The amorphous fraction is progressively reduced when the Al content is increased. As-spun ribbons showed a ductile fracture behavior, coupled with high hardness values (260–290 HV).

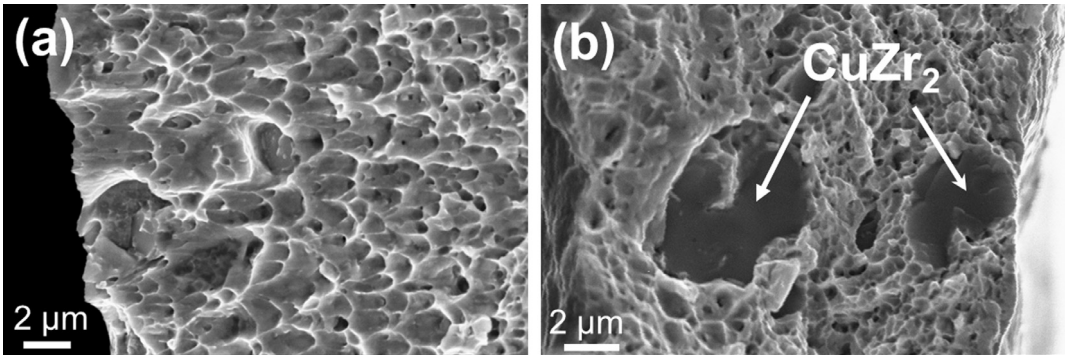

Fig. 5. SEM micrographs (secondary electron signal) of the fracture surfaces for the ribbons of alloy B0 (a) and alloy B1 (b) after tensile test.

Acknowledgements

The authors acknowledge financial support by MIUR (PRIN 2008).

References

[1] S. Curiotto, N.H. Pryds, E. Johnson, L. Battezzati, Metall. Mater. Trans. A 37 (2006) 2361–2368.
[2] H. Okamoto, Phase Diagrams for Binary Alloys, ASM International, Materials Park (OH), 2000.
[3] R.D. Doherty, in: R.W. Cahn, P. Haasen (Eds.), Physical Metallurgy, vol. 2, North Holland, Amsterdam, 1996, pp. 1480–1490.
[4] R.N. Singh, F. Sommer, Rep. Prog. Phys. 60 (1997) 57–150.
[5] A.A. Kündig, M. Ohnuma, D.H. Ping, T. Ohkubo, K. Hono, Acta Mater. 52 (2004) 2441–2448.
[6] H.J. Chang, W. Yook, E.S. Park, J.S. Kyeong, D.H. Kim, Acta Mater. 58 (2010) 2483–2491.
[7] E.S. Park, E.Y. Jeong, J.K. Lee, J.C. Bae, A.R. Kwon, A. Gebert, L. Schultz, H.J. Chang, D.H. Kim, Scripta Mater. 56 (2007) 197–200.
[8] A. Gebert, N. Mattern, U. Kühn, J. Eckert, L. Schultz, Intermetallics 15 (2007) 1183–1189.
[9] J. Jayaraj, B.J. Park, D.H. Kim, W.T. Kim, E. Fleury, Scripta Mater. 55 (2006) 1063–1066.
[10] C.C. Hays, C.P. Kim, W.L. Johnson, Mater. Sci. Eng. A 304–306 (2001) 650–655.
[11] E. Pekarskaya, C.P. Kim, W.L. Johnson, J. Mater. Res. 9 (2001) 2513–2518.
[12] C.A. Schuh, T.C. Hufnagel, U. Ramamurty, Acta Mater. 55 (2007) 4067–4109.
[13] G.Y. Sun, G. Chen, C.T. Liu, G.L. Chen, Scripta Mater. 55 (2006) 375–378.
[14] A. Castellero, T. Baser, J. Das, P. Matteis, J. Eckert, L. Battezzati, M. Baricco, J. Alloys Comp. 509 (2011) S99–S104.
[15] A. Inoue, W. Zhang, T. Tsurui, A.R. Yavari, A.L. Greer, Phil. Mag. Lett. 85 (2005) 221–229.
[16] A. Castellero, S.J. Lloyd, S.V. Madge, Z. Kovacs, J.F. Löffler, M. Baricco, A.L. Greer, J. Alloys Comp. 434–435 (2007) 48–51.
[17] D.H. Kang, I.-H. Jung, Intermetallics 18 (2010) 815–833.
[18] D. Janovszky, K. Tomolya, A. Sycheva, G. Kaptay, J. Alloys Comp. 541 (2012) 353–358.
[19] A. Castellero, D.H. Kang, I.-H. Jung, G. Angella, M. Vedani, M. Baricco, J. Alloys Comp. 536 (2012) S148–S153.
[20] W. Zhang, A. Inoue, J. Mater. Res. 21 (2006) 234–241.
[21] A.A. Kündig, M. Ohnuma, T. Ohkubo, T. Abe, K. Hono, Scripta Mater. 55 (2006) 449–452.
[22] K. Tretyachenko, in: G. Effenberg, S. Ilyenko (Eds.), Aluminium–Copper–Zirconium. The Landolt–Börnstein Database – Group IV Physical Chemistry, vol. 11A2, Springer, 2005, pp. 206–222.
[23] B.W. Zhou, X.G. Zhang, W. Zhang, H. Kimura, T. Zhang, A. Makino, A. Inoue, Mater. Trans. 51 (2010) 826–829.
[24] D. Wang, Y. Li, B.B. Sun, M.L. Sui, K. Lu, E. Ma, Appl. Phys. Lett. 84 (2004) 4029–4031.
[25] G.I. Taylor, Proc. R. Soc. Lond. 146 (1934) 501–523.
[26] D. Lussana, A. Castellero, D. Ripamonti, G. Angella, M. Vedani, A. Zambon, M. Baricco, Int. J. Mat. Res. 103 (2012) 1117–1121.